Journal of Hazardous Materials 514 (2026) 142872

Contents lists available at ScienceDirect

Journal of Hazardous Materials

journal homepage: www.elsevier.com/locate/jhazmat

Weathering of nanoplastics reduces the effect of sand surface heterogeneity on their attachment in saturated porous media

Yanghui Xu [a,b], Jan Peter van der Hoek [b,c], Luuk C. Rietveld [b], Gang Liu [a,b,d,*], Kim Maren Lompe [b]

[a] Key Laboratory of Drinking Water Science and Technology, Research Centre for Eco-Environmental Sciences, Chinese Academy of Sciences, Beijing 100085, China
[b] Section of Sanitary Engineering, Department of Water Management, Faculty of Civil Engineering and Geosciences, Delft University of Technology, Stevinweg 1, Delft 2628 CN, the Netherlands
[c] Waternet, Department Research & Innovation, P.O. Box 94370, Amsterdam 1090 GJ, the Netherlands
[d] University of Chinese Academy of Sciences, Beijing 100049, China

HIGHLIGHTS

- Sand physicochemical heterogeneity caused two-stage NP transport dynamics.
- NPs initially filled heterogeneous sand sites, then attached to smoother areas.
- Early retardation was driven by rapid irreversible with minor reversible attachment.
- Weathering of NPs masked heterogeneity effects and weakened initial retardation.
- NOM molecular weight governed attachment of non- and UV-weathered NPs..

GRAPHICAL ABSTRACT

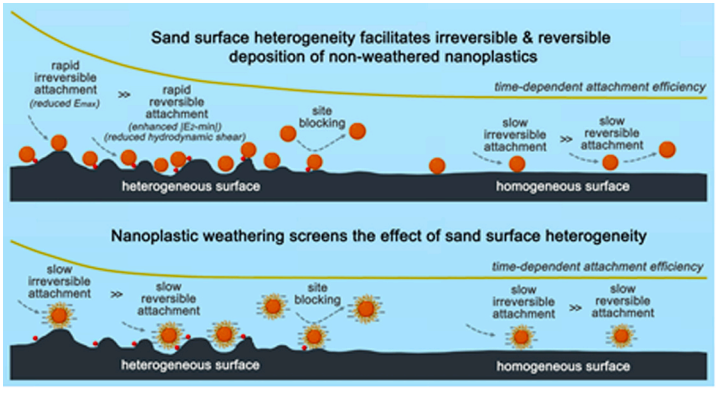

ARTICLE INFO

Keywords:
Site blocking
Retardation
Surface heterogeneity
UV weathering
Natural organic matter

ABSTRACT

The deposition of nanoplastics (NPs) in porous media is strongly influenced by natural weathering processes, such as UV exposure and adsorption of natural organic matter (NOM), but the deposition mechanisms of both, non-weathered and weathered NPs, remain poorly understood. In this study the effect of NOM on the transport of non-weathered polystyrene (PS) NPs and UV-weathered PS NPs was examined in saturated porous media under low ionic strength conditions. It revealed that the physical and chemical heterogeneity of the sand surface created favorable attachment sites, leading to site blocking and retardation of NPs. NPs followed a non-steady-state, two-stage transport dynamic: rapid, irreversible, and reversible or pseudo-equilibrium attachment on heterogeneous areas until site saturation, followed by slow, irreversible attachment on relatively homogeneous surfaces. Both UV weathering and NOM coating generated more negatively charged NPs, reducing the irreversible and reversible deposition of NPs. These weathering processes reshaped NP transport dynamics and

* Correspondence to: Research Center for Eco-Environmental Sciences, Chinese Academy of Sciences, Sanitary Engineering, CiTG, Delft University of Technology, the Netherlands.
E-mail addresses: gliu@rcees.ac.cn, g.liu-1@tudelft.nl (G. Liu).

https://doi.org/10.1016/j.jhazmat.2026.142872
Received 21 March 2026; Received in revised form 14 May 2026; Accepted 30 June 2026
Available online 7 July 2026

masked the retardation effects induced by sand surface heterogeneity. Moreover, the impact of NOM on NP deposition varied depending on the extent of UV weathering and the molecular weight of the NOM.

1. Introduction

Microplastics have been widely studied due to their persistence and ecological toxicity [1,2]. More recently, nanoplastics (NPs, <1 μm) have gained increasing attention [3,4]. NPs originate from two main sources: primary NPs, which are intentionally manufactured for commercial and industrial applications [5], and secondary NPs that are formed through the degradation of larger plastic particles, e.g. by UV-induced breakdown [6]. NPs have been detected in various water sources, including surface water, groundwater, and riverbank filtrate (RBF) [7]. Especially, the presence of NPs in RBF raises concerns about its effectiveness in removing these particles.

Studies on NP transport and deposition often draw upon established knowledge of colloid transport in porous media [8]. The classical clean bed filtration theory (CFT) is the most commonly used approach for describing the filtration of colloidal particles [9]. The CFT assumes that collector surfaces are perfectly smooth and uniformly charged, with the deposition rate being constant. A first-order kinetic model is typically employed to describe deposition, where colloids break through without retardation (i.e., breakthrough occurs at or before the first pore volume) and the breakthrough curve (BTC) remains a steady-state plateau [10]. The classic Derjaguin-Landau-Verwey-Overbeek (DLVO) theory is commonly used to explain the deposition phenomena [11]. However, non-steady-state breakthrough, driven by mechanisms such as site blocking, is commonly seen in experiments [12,13]. This is usually explained by the physical and chemical heterogeneity of the collector surface, resulting in varying deposition rates [10,14]. Particularly retardation, which deviates from the CFT, has been observed in the case of colloids [15,16]. While retardation is associated with "equilibrium adsorption" during the transport of reactive solutes [17], this concept cannot directly be applied to colloid transport as colloids are typically thermodynamically unstable [18]. Despite these advances, the mechanisms governing retardation and non-steady-state breakthrough in porous media remain poorly understood.

The transport of NPs in porous media has extensively been studied using commercially available NPs, such as PS NPs [19–27]. Natural weathering processes, including UV irradiation and eco-corona formation via adsorption of natural organic matter (NOM), can modify NP surface properties and thereby influence their transport behavior [19,22,23,25–27]. For instance, some authors have reported that NOM adsorption can enhance NP transport by increasing electrostatic repulsion [23,26], or by inducing additional steric repulsion [19,27]. However, weathering processes may not only enhance the transport capacity of NPs, but may also lead to distinct transport dynamics. Non-steady-state breakthrough and retardation, deviating from CFT, are often observed during transport of non-weathered NPs, whereas weathered NPs tend to show steady-state breakthrough with reduced or negligible retardation compared to pristine particles [27,28]. Despite these observations, this aspect has not been explicitly studied. Overall, the mechanisms behind these deviations from CFT, as well as how weathering reshapes NP transport dynamics in porous media, remain unclear.

Therefore, the main objective of this study is to elucidate the mechanisms of controlling the transport dynamics of non-weathered and weathered NPs in saturated porous media. Commercial PS NPs, representing non-weathered NPs, were UV-aged using a mercury lamp to produce UV-weathered PS NPs. Suwanee River NOM was incubated with both non-weathered and UV-weathered PS NPs to generate NOM-adsorbed NPs. NOM was further split into different MW fractions to study how NOM size modifies NPs and affects their deposition. BTCs for non-weathered and weathered NPs in saturated porous media were obtained by filtering over clean quartz sand columns. Finally, a two-site kinetic model and an equilibrium-kinetic model, combined with DLVO and extended DLVO (XDLVO) theory, were used to elucidate the mechanisms driving the deposition of non-weathered and weathered NPs.

2. Materials and methods

2.1. Materials

A PS stock solution with a concentration of 50% w/v and a nominal NP size of 100 nm was obtained from Zhichuan Intelligent Technology (Suzhou, China) Co., Ltd. The PS NPs were unfunctionalized but contained the surfactant sodium dodecyl sulfate (SDS), as specified by the manufacturer. To minimize interference from SDS, the PS suspension (5 g/L) underwent four rounds of washing with ultrapure water via ultracentrifugation (22000 × g, 30 min) and sonication (40 kHz, 5 min) until the total organic carbon (TOC) in the supernatant water was reduced to near the level of quantification (0.38 ± 0.11 mg C/L). The cleaning process did not lead to NP aggregation, as found in our previous study [29]. Suwannee River NOM was purchased from the International Humic Substances Society. Polyvinylidene fluoride (PVDF) ultrafiltration membranes with cutoff sizes of 0.05 μm, 30 kDa, 10 kDa, and 3 kDa were acquired from RisingSun Membrane Technology (Beijing, China) Co., Ltd to separate NOM fractions based on molecular weight.

The used quartz sand had a diameter of 0.4–0.8 mm, and was purchased online from vidaXL. For comparison, two other types of quartz sand were obtained from Sigma-Aldrich: Sigma−1, with a size range of 0.2–0.8 mm, and Sigma−2 with a narrower range of 0.21–0.30 mm. The vidaXL sand and the Sigma−1 sand were then sieved using stainless steel screens (30 and 40 mesh) to obtain 0.425–0.6 mm vidaXL sand, 0.425–0.6 mm Sigma−1 sand, and 0.2–0.425 mm Sigma−1 sand. The sand was then cleaned to remove possible organic residues and metals by sequentially soaking it in concentrated NaOH for 24 h, followed by washing with concentrated HCl for 24 h. After cleaning, the sand was thoroughly rinsed with ultrapure water until the pH stabilized at approximately 6.5. Finally, the cleaned quartz sand was heated at 550 °C for 5 h.

2.2. Preparation of weathered nanoplastics

The UV-weathered PS NPs were prepared in ultrapure water by exposing 300 mg/L PS NPs to a 500 W mercury lamp (35 mW/cm^2) for 2, 4 and 8 days [29]. Detailed procedures are provided in Text S1 and Figure S1. The pristine and UV-weathered NPs are denoted as PS_0, PS_2, PS_4, and PS_8, respectively. The particle number concentrations of both pristine and UV-weathered NPs were assumed to remain unchanged, as UV aging did not result in obvious fragmentation of the NPs (Figure S2). After the aging process, the UV-weathered NPs were washed four times with ultrapure water using ultracentrifugation (Eppendorf, Centrifuge 5910 Ri, 22000 × g, 30 min) and sonication (DK-3000H, 40 kHz, 5 min) to remove any leached dissolved organic carbon from plastic photodegradation. To account for changes in NP concentration during washing, the concentration of washed weathered NPs was adjusted to match the UV absorbance at 289 nm (UV_{289}) of unwashed aged NPs. At a concentration of 10 mg/L, pristine PS_0 exhibited a UV_{289} absorbance of 0.952 cm^{-1}, corresponding to approximately 4.68 × 10^{12} particles/L. For the same particle number concentration (~4.68 × 10^{12} particles/L), the UV_{289} values of aged PS_2, PS_4, and PS_8 decreased to 0.927 cm^{-1}, 0.916 cm^{-1}, and 0.902 cm^{-1}, respectively. The TOC concentrations for PS_0, PS_2, PS_4, and PS_8 at this particle concentration were 29.2 mg C/L,

26.8 mg C/L, 24.7 mg C/L, and 23.6 mg C/L, respectively (Table S1). For the transport experiments, the pristine (PS_0) and UV-weathered NPs (PS_2, PS_4, PS_8) were diluted to 4.68×10^{12} particles/L in a 10 mM NaCl solution. 10 mM NaCl was selected to represent a typical surface water with low ionic strength. The pH was adjusted to 6.0 ± 0.1 using 0.1 M HCl or NaOH to reflect environmentally relevant conditions [30,31]. As this pH was close to the initial pH of the diluted NP suspensions, only minimal adjustment was required.

NOM-adsorbed NPs were prepared by mixing the Suwannee River NOM (2 mg C/L) with either 4.68×10^{12} particles/L pristine or UV-weathered NPs in 10 mM NaCl, with the pH adjusted to 6.0 ± 0.1. Relatively high NP concentrations were used, to avoid NOM's influence on UV_{289} for NPs' measurement. NOM with a size below 0.05 μm, which represents the majority of total NOM [32,33], was selected for easy separation from the larger NPs after the adsorption experiment using 0.1 μm filters. NOM was further fractionated by ultrafiltration to obtain size-defined fractions based on molecular weight, as detailed in Text S2. The prepared concentrations were as follows: 343 mg/L for bulk NOM (< 0.05 μm), 244 mg/L for NOM (30 kDa–0.05 μm), 101 mg/L for NOM (10–30 kDa), 243 mg/L for NOM (3–10 kDa), and 131 mg/L for NOM (< 3 kDa). To obtain stable NOM-adsorbed NPs, the mixture was allowed to react for 24 h to reach equilibrium [29]. The adsorption of NOM by NPs was further tested, as described in Text S3, Figure S3 and S4.

2.3. Column transport experiments

Polymethyl methacrylate column with a height of 9 cm and an inner diameter of 2 cm was used to study NP transport in the porous media (see the setup in Figure S4). The ratio between the column diameter and sand grain diameter was 33, which falls within the recommended range of 20–50, ensuring minimal wall effects and preferential flow paths [34]. To prevent sand loss from the bottom and ensure a uniform flow distribution at the top, a stainless steel mesh with a 200 μm opening was placed at the bottom of the column. During sand packing, ultrapure water was introduced from the bottom of the column. The cleaned, dry sand was then wetted with ultrapure water, and gradually added to the column using a spoon and while gently stirring the column to prevent layering and air entrapment. The resulting sand bed porosity was 0.39, calculated based on the inserted sand mass, the packed column volume, and a sand density of 2.56 g/cm^3. After packing, several pore volumes (PVs) of ultrapure water were injected to wash the sand in the columns. 10 mM NaCl was used as a tracer to assess the conservative transport properties of the packed columns, while measuring the electrical conductivity with a potable conductivity meter (HQ1140, HACH, USA) in the effluents of the column. As for all experiments, a constant flow of 1 mL/min (0.54 m/h) was applied in an upward direction, using a peristaltic pump (Longer BT100–3J).

For NP transport studies, the columns were pre-flushed with a particle-free background electrolyte (10 mM NaCl) for 10 PVs to establish stable baseline conditions. Following this, 25 or more PVs of NP suspension were injected, followed by 10 PVs of background electrolyte elution to allow the column effluent UV_{289} to return to baseline levels. Effluent samples were collected in glass tubes from the top of the column at equal time intervals to obtain BTCs. NP concentrations were measured using a UV spectrophotometer (G10S UV-Vis, Thermo Fisher Scientific) at a wavelength of 289 nm. For NPs in the presence of NOM, the UV_{289} was corrected by subtracting the contribution of non-adsorbed NOM. Transport experiments for pristine NPs were conducted at concentrations of 2 mg/L (9.36×10^{11} particles/L, UV_{289}=0.211 cm^{-1}), 5 mg/L (2.34×10^{12} particles/L, UV_{289}=0.505 cm^{-1}), and 10 mg/L (4.68×10^{12} particles/L, UV_{289}= 0.952 cm^{-1}) in 10 mM NaCl. For UV-weathered and NOM-adsorbed NPs' transport studies, 4.68×10^{12} particles/L in 10 mM NaCl was used. Both non-weathered and weathered NPs were pre-equilibrated for 24 h before injection. NP aggregation was not observed after the 24-h reaction period, as indicated by dynamic light scattering measurements. Either duplicate or triplicate experiments were conducted for each transport condition.

2.4. Adsorption and desorption experiments

Batch adsorption experiments were conducted to study the adsorption of non-weathered and weathered NPs by the cleaned 0.425–0.600 mm vidaXL sand. A 100 mL suspension of 4.68×10^{12} particles/L (UV_{289}= 0.952 cm^{-1}) of either non-weathered or weathered NPs was mixed with 50 g of sand in 10 mM NaCl. The mixture was agitated at 160 rpm for 48 h. The suspension was sampled at specific time intervals (0, 1, 2, 10 min and 0.5, 2.5, 20, 24 and 48 h) and tested for UV_{289}. After 48 h, the suspension was replaced with 85 mL of particle-free 10 mM NaCl solution, and the desorption of NPs was tested at several time intervals (0, 1, 2, 10, and 30 min). Controls, without sand addition, showed no obvious UV_{289} reduction of NPs following agitation for 48 h (Figure S5). Blanks, without NP addition, indicated that agitation caused the fragmentation and release of suspended fine sands, which interfered with the UV_{289} for NPs' measurement (Figure S6). The UV_{289} of NPs was corrected by subtracting the blank UV_{289} measured at the same time. Detailed analysis results are presented in Text S4.

2.5. Characterization

The hydrodynamic size and zeta potential of non-weathered and weathered NPs were measured using a Zetasizer Nano ZS90 (Malvern Instruments, UK). The size and morphology of the pristine and UV-weathered NPs in ultrapure water were analyzed using a scanning electron microscope (SEM, Quattro, FEI). To detect surface functional groups of NPs, attenuated total reflectance Fourier transform infrared spectroscopy (ATR-FTIR, Nicolet iN10, Thermo Fisher Scientific) was used, covering wavenumbers from 400 to 4000 cm^{-1}. The pristine and UV-weathered PS NPs samples were prepared by drying concentrated NPs on a glass slide at 40°C, while NOM samples were freeze-dried using a freeze-dryer (BK-FD12PT, BIOBASE BIODUSTRY) prior to FTIR analysis. The zeta potential of the used sands was also characterized using a Zetasizer Nano ZS90. Prior to testing, the sands were ground into fine particles using a stainless steel rod to facilitate suspension and measurement [35].

The surface morphology of the sand and the deposited NPs was characterized using both an optical microscope and SEM. Energy-dispersive X-ray spectroscopy (EDX; EDX1800ROHS) was conducted to identify the major elemental components present on the sand surfaces. In addition, X-ray diffraction (XRD; PHILIPS PW 1710) was used to analyze the mineralogical composition of the sands.

2.6. Modelling

In porous media, the transport and deposition of NPs are primarily controlled by three major processes: advection, dispersion, and attachment/detachment to/from collector surfaces. These processes are typically described by 1-D advection-dispersion-reaction (ADR) equation:

$$\frac{\partial C}{\partial t} = D\frac{\partial^2 C}{\partial z^2} - \nu\frac{\partial C}{\partial z} - \frac{\rho_b}{\theta}\frac{\partial S}{\partial t} \quad (1)$$

Where t represents time (min), z is the distance (cm), C denotes the concentration of NPs in solution (mg/L or particle/L), D is the hydrodynamic dispersion coefficient (cm^2/min), ν is the average pore water flow velocity (cm/min), ρ_b is the sand bulk density (mg/cm^3),θ is the porosity of the sand media (dimensionless), and S (mg/kg) denotes the concentration of NPs on the sand due to deposition. The mean pore-water flow velocity and the hydrodynamic dispersion coefficient used in NP simulations were obtained by fitting to a NaCl tracer breakthrough curve.

The reaction term $\frac{\rho_b}{\theta}\frac{\partial S}{\partial t}$ in the transport equation can further be

described using a first-order reversible kinetic model, which is expressed as follows [36]:

$$\frac{\rho_b}{\theta}\frac{\partial S}{\partial t} = k_{att}\psi C - \frac{\rho_b}{\theta}k_{\det}S \quad (2)$$

Where k_{att} (min^{-1}) is the first-order attachment coefficient, k_{det} (min^{-1}) is the first-order detachment coefficient (equal to 0 for irreversible retention), and ψ is a variable depending on the attachment mechanisms being modeled. The following three attachment models were considered in this study to simulate the experimental results [12].

(1) Clean bed filtration (CFT) model.
The function ψ in the attachment term is 1 for CFT. Under steady-state flow conditions, the NP attachment rate k_{att} in the attachment term can be expressed as below:

$$k_{att} = \frac{\nu}{L}\ln(\frac{C_0}{C}) \quad (3)$$

Where L is the column length (cm), C_0 and C represent the influent and steady-state effluent NP concentrations (mg/L), respectively. The steady-state concentration C is used to evaluate the retention of NPs in the column during CFT. The obtained first-order attachment rate coefficient k_{att} (min^{-1}) can then be used to calculate the attachment efficiency α (dimensionless), the ratio of particles attached to the collector to all particles colliding with the collector, using the following equation [16]:

$$\alpha = \frac{2k_{att}d_c}{3(1-\theta)\nu\eta_0} \quad (4)$$

Where d_c is the diameter of sand grain (cm), and η_0 is the single collector efficiency (dimensionless), calculated using the Tufenkji-Elimelech equation [37].

(2) Site blocking. The clean bed with site-blocking model includes a maximum retention capacity, S_{max} (μg/g), to limit NP deposition [12]. This is represented by the following equation:

$$\psi = 1 - \frac{S}{S_{\max}} \quad (5)$$

In this model, ψ is a dimensionless Langmuirian blocking function. When the retention capacity S_{max} is much larger than S, ψ approaches 1, and Eq. (2) simplifies to CFT model. As NP attachment increases and S approaches S_{max}, the ψ approaches zero.

To study the presence of multiple kinetic deposition sites, a two-site kinetic model was employed to fit the BTCs using HYDRUS 1-D. This model accounts for both reversible and irreversible kinetic attachment at two different sites, as described by the equation below [14]:

$$\frac{\rho_b}{\theta}\frac{\partial(S_1+S_2)}{\partial t} = k_{a1}\psi_1 C + k_{a2}\psi_2 C - \frac{\rho_b}{\theta}k_{d1}S_1 \quad (6)$$

$$\psi_1 = 1 - \frac{S_1}{S_{\max 1}} \quad (7)$$

$$\psi_2 = 1 - \frac{S_2}{S_{\max 2}} \quad (8)$$

Where S_1 (μg/g) and S_2 (μg/g) are the solid phase NP concentrations on site 1 and site 2, respectively, k_{a1} (min^{-1}) and k_{a2} (min^{-1}) are the attachment rate coefficient for site 1 and site 2, respectively. S_1 was assumed to be the preferential attachment site. Therefore, k_{a1} at S_1 was set a value one order of magnitude higher than k_{a2} at S_2, capturing a fast initial attachment phase followed by slower subsequent attachment. Sensitivity analysis showed that k_{a1} mainly influenced the initial retardation, while k_{a2} governed the plateau in the later stage of the BTCs. k_{d1} is the detachment rate at site 1 while the attachment at site 2 was assumed to be irreversible [14]. ψ_1 and ψ_2 represent dimensionless Langmuirian blocking functions at site 1 and site 2, respectively, while S_{max1} (μg/g) and S_{max2} (μg/g) denote the maximum retention capacities at these sites.

(3) Combined kinetic and equilibrium model. A combined model containing a first-order kinetic component (S_k) and an equilibrium component (S_e), in accordance with a linear Freundlich isotherm, can be written as:

$$\frac{\rho_b}{\theta}\frac{\partial(S_k+S_e)}{\partial t} = k_{att}C - \frac{\rho_b}{\theta}k_{\det}S \quad + K_d\frac{\rho_b}{\theta}\frac{\partial C}{\partial t} \quad (9)$$

.

When the kinetic detachment term (k_{det}) is neglected, and first-order attachment was assumed to be irreversible, the equilibrium component could then be incorporated into 1-D advection-dispersion-reaction (ADR) Eq. (1):

$$(1 + K_d\frac{\rho_b}{\theta})\frac{\partial C}{\partial t} = \quad D\frac{\partial^2 C}{\partial z^2} - \quad \nu\frac{\partial C}{\partial z} - k_{att}C \quad (10)$$

$$\mathrm{R} = 1 + K_d\frac{\rho_b}{\theta} \quad (11)$$

Where R is the retardation factor and K_d is the distribution coefficient.

Introducing K_d in NP transport modeling simplifies the attachment/detachment process by reducing the parameters. However, conceptually, the equilibrium assumption is invalid because K_d is fundamentally based on Gibbs energy and the assumption of thermodynamic equilibrium, whereas NPs are inherently thermodynamically unstable [18]. On the other hand, several authors have successfully applied the concept of K_d in modeling NP transport [8,38–40], aligning with other experimental studies that observe retarded BTCs [14,41]. In this study, "equilibrium retention" of NPs was observed based on the adsorption and desorption experiments, along with obvious retardation in the BTCs of PS NPs. Therefore, the equilibrium-kinetic model incorporating the distribution coefficient (K_d) and retardation factor (R) was also considered to fit the BTCs using STANMOD software.

2.7. DLVO and XDLVO interaction energy

The classical DLVO theory, which accounts for Van der Waals attraction and electrostatic double-layer repulsion, was applied to describe the interaction energies between NPs and sand [42,43]. In the presence of NOM, the extended DLVO (XDLVO) theory was employed to incorporate steric repulsion when evaluating the interaction energies between NPs and sand surfaces. Surface physical heterogeneity or roughness (Figure S7), and chemical heterogeneity were also considered in the DLVO and XDLVO interaction calculation [44,45]. Detailed calculations are provided in Text S7, Table S2 and S3.

3. Results and discussion

3.1. Two-stage deposition of nanoplastics

The BTCs of 2, 5 and 10 mg/L PS NPs, along with the corresponding total input mass and cumulative breakthrough mass profiles during a single pulse under 10 mM NaCl are depicted in Fig. 1. The BTC of the tracer (10 mM NaCl) in the column showed distinct single peaks (Figure S8), suggesting that NaCl behaved as a non-reactive tracer, confirming that the sand-packed column was properly prepared. In contrast with most previous studies, where NP BTC was typically observed after only a few PVs [24,25], NP suspensions in this study were

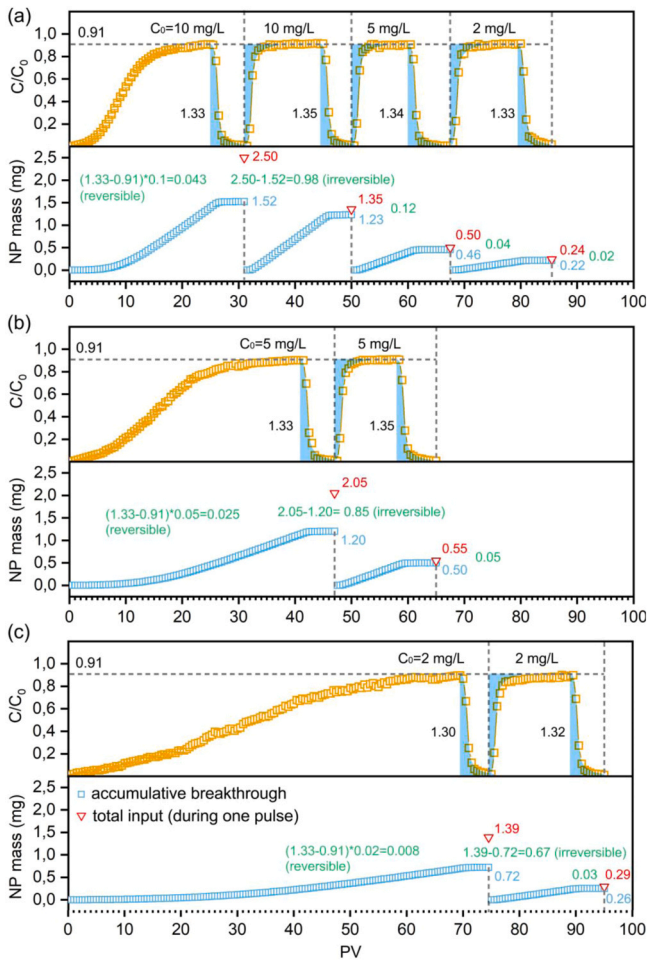

Fig. 1. The BTCs (yellow dots), total input NP mass (red dots), and accumulative breakthrough mass profiles (blue dots) of 2, 5 and 10 mg/L non-weathered NPs during a single pulse in 10 mM NaCl. The red, blue, and green numbers indicate the total input NP mass (mg), total NP breakthrough (mg), and total retention (mg), respectively, during a single pulse. The shaded area under the tail of the curve represents the normalized NP concentration during the elution stage, which is symmetric to the shaded region during initial ascent stage. Error bars represent the mean ± range (minimum to maximum) (n = 2).

injected for 25 PVs, to observe the full breakthrough. This study revealed an S-shaped breakthrough pattern: the BTCs of NPs in the first pulse exhibited an initial retardation, followed by a rapid increase, and then a gradual rise until eventually flattening at $C/C_0 = 0.91$ (Fig. 1a). Also, at lower NP concentrations, the initial NP breakthrough curve was S-shaped but the plateau of constant NP effluent concentration was reached later (Figs. 1b and 1c). Correspondingly, the cumulative breakthrough mass profiles showed a negligible NP breakthrough in the initial stage, followed by a gradual, linear increase at a near-constant rate until the start of the elution stage.

The elution stage with NP-free solution should theoretically result in a washout of C/C_0*PV = 0.91 (representing the mass of NPs in 1 PV of water) if no detachment occurs. However, the integrated areas under the elution curves during the first pulse were C/C_0*PV = 1.30–1.33 at different NP input concentrations, suggesting that only a small part of the NPs underwent reversible attachment. This observation is consistent with the results of the batch experiments, where NPs were detached upon replacement with NP-free solution (Text S4 and Figure S6). By subtracting the total breakthrough (including the elution stage) from the total mass input, the retained NPs were attributed to irreversible attachment. The mass of irreversibly attached NPs was calculated to be in pulse 1 a (2.50 mg – 1.52 mg =) 0.98 mg, pulse 1 b (2.05 mg – 1.20 mg =) 0.85 mg, and pulse 1 c (1.39 mg – 0.72 mg =) 0.67 mg for input concentrations of 10 mg/L, 5 mg/L, and 2 mg/L, respectively. These results demonstrate that both reversible and irreversible NP attachment are concentration-dependent processes, with irreversible attachment predominating during the first pulse.

Unlike the first pulse BTCs, all concentrations of NPs in the second and subsequent pulses exhibited approximately an expected breakthrough: no noticeable retardation (noticeably breaking through at the first PV) and quickly leveled off at the same plateau (i.e., 0.91) (Fig. 1). The shaded area under the tail of the curve in the elution stage mirrored that observed during the initial ascent, indicating symmetry between the initial injection and the final elution. This breakthrough pattern is consistent with the principles of traditional CFT that assumes a constant attachment rate under steady-state conditions [12]. Furthermore, the integrated areas under the elution curves during the second and subsequent pulses showed little change compared to the elution stage of the first pulse. This suggests that the amount of reversibly attached NPs remained relatively constant and low between pulses, indicating that NP attachment was predominantly irreversible, and reversible attachment mainly occurred during the initial stage of transport.

Physical straining and site blocking are commonly cited mechanisms explaining the deviation of colloid transport from CFT [8]. Straining refers to the trapping of relatively large particles, where the ratio of particle radius to the median collector radius exceeds 0.0017, within pore throats [46]. As higher concentrations may lead to more colloid aggregation and increased particle size, straining typically results in decreased transport of colloids as the input concentration increases [47]. In this study, PS NPs had a size ratio to sand grains of about 0.0003, showed no aggregation, and demonstrated an opposite concentration-dependent transport behavior, suggesting straining was not the deposition mechanism of PS NPs. Therefore, to study site blocking, a modeling approach (Eq. 5) was adopted where a maximum solid phase concentration (S_{max}) was added to constrain the NP deposition. As NP attachment increases over time, the available sites on the collector surface are gradually covered by the deposited NPs (as S approaches S_{max}), leaving fewer sites available for further deposition [12]. Typically, increasing the input concentration of particles facilitates their transport, as higher input concentrations lead to greater surface coverage and faster site saturation [48–50]. Therefore, in this study, site blocking might be responsible for the time-dependent and concentration-dependent deposition of PS NPs in the first pulse.

However, the one-site model, both with and without the Langmuirian blocking function, did not adequately fit the entire BTCs in the first pulse (Figure S9). On the other hand, the two-site kinetic model with a Langmuirian blocking function for each site provided a good fit for all the BTCs (Figure S9). The value of the attachment coefficient k_{a1} was approximately one order of magnitude larger than k_{a2} for PS NPs (Table 1), indicating that NP deposition was dominated by fast deposition at site 1. The time retardation of BTCs was predominantly determined by the values of k_{a1} and S_{max1}. A higher value of k_{a1} indicates a more favorable deposition, leading to complete retention until the solid phase concentration of NPs at site 1 approached S_{max1}. The above analysis indicates that some reversible attachment could occur during the initial stage of transport; therefore, the detachment rate constant k_{d1} was incorporated in the two-site blocking model. The fitted values showed that k_{d1} was approximately one order of magnitude lower than k_{a1} (Table 1), suggesting that the attachment process dominated over detachment at site 1 during NP filtration, until saturation. In the batch experiments, the rapid attachment of PS NPs by sand during the initial mixing stage (< 10 min), along with rapid detachment (Figure S6), was consistent with rapid attachment during the first NP injection and fast detachment during the initial elution stage in the transport experiments, suggesting that breakthrough curve can be approximated with a model that uses equilibrium processes [51,52]. Additionally, the observed initial retardation followed by e breakthrough supports the use of an

Table 1
The average effluent concentration, attachment efficiency, and the fitted parameters using two-site kinetic model and equilibrium-kinetic model. C/C_0 and C_2/C_0 are the overall and steady-state plateau average effluent concentrations, respectively. α and α_2 are the overall and steady-state attachment efficiency, respectively. α_1 (= α - α_2) represents the attachment efficiency before steady-state plateau.

	C/C_0	α	C_2/C_0	α_2	α_1	S_{max1} (μg/g)	k_{a1} (min^{-1})	k_{d1} (min^{-1})	S_{max2} (μg/g)	k_{a2} (min^{-1})	R	K_d (mL/g)	k_{att} (min^{-1})
PS_0	0.559	9.40E−02	0.912	1.49E−02	7.91E−02	8.84	1.038	0.104	0.632	2.15E−02	10.03	2.153	9.93E−03
PS_0 + bulk	0.814	3.29E−02	0.979	3.38E−03	2.95E−02	0.72	0.266	0.039	0.161	3.88E−03	3.64	0.629	2.41E−03
PS_0 + > 30 kDa	0.826	3.03E−02	0.974	4.11E−03	2.62E−02	0.97	0.267	0.097	0.185	9.57E−03	3.24	0.534	3.36E−03
PS_0 + 10–30 kDa	0.780	3.98E−02	0.964	5.93E−03	3.39E−02	1.07	0.315	0.062	0.256	9.99E−03	4.01	0.718	4.55E−03
PS_0 + 3–10 kDa	0.767	4.28E−02	0.964	5.97E−03	3.69E−02	1.32	0.426	0.083	0.276	7.94E−03	4.26	0.776	4.82E−03
PS_0 + < 3 kDa	0.752	4.62E−02	0.960	6.58E−03	3.97E−02	1.53	0.475	0.096	0.309	8.37E−03	4.49	0.832	5.34E−03
PS_2	0.681	6.48E−02	0.958	7.29E−03	5.75E−02	6.12	0.464	0.017	0.391	1.85E−02	7.46	1.540	5.28E−03
PS_2 + bulk	0.798	3.76E−02	0.972	4.69E−03	3.29E−02	0.91	0.314	0.044	0.324	4.94E−03	3.82	0.672	4.34E−03
PS_2 + > 30 kDa	0.813	3.43E−02	0.971	4.80E−03	2.95E−02	0.92	0.292	0.062	0.340	6.83E−03	3.40	0.573	4.66E−03
PS_2 + 10–30 kDa	0.786	3.97E−02	0.970	5.11E−03	3.46E−02	0.81	0.331	0.032	0.337	7.58E−03	3.94	0.701	4.76E−03
PS_2 + 3–10 kDa	0.759	4.59E−02	0.966	5.73E−03	4.01E−02	1.11	0.509	0.063	0.303	9.85E−03	4.46	0.825	5.12E−03
PS_2 + < 3 kDa	0.748	4.86E−02	0.960	6.77E−03	4.18E−02	0.82	0.321	0.079	0.372	8.45E−03	4.66	0.874	4.93E−03
PS_4	0.723	5.71E−02	0.961	7.09E−03	5.00E−02	3.01	0.328	0.024	0.310	4.85E−03	6.76	1.373	2.83E−03
PS_4 + bulk	0.781	4.26E−02	0.961	6.76E−03	3.58E−02	1.70	0.452	0.115	0.331	6.97E−03	3.99	0.712	4.13E−03
PS_4 + > 30 kDa	0.797	3.91E−02	0.961	6.78E−03	3.23E−02	1.16	0.322	0.098	0.332	1.32E−02	3.47	0.589	5.70E−03
PS_4 + 10–30 kDa	0.776	4.37E−02	0.962	6.62E−03	3.71E−02	0.79	0.342	0.035	0.308	1.14E−02	4.03	0.722	5.12E−03
PS_4 + 3–10 kDa	0.755	4.92E−02	0.963	6.56E−03	4.26E−02	1.25	0.580	0.084	0.269	1.08E−02	4.51	0.837	4.82E−03
PS_4 + < 3 kDa	0.715	5.92E−02	0.962	6.90E−03	5.22E−02	3.06	0.681	0.136	0.330	1.36E−02	5.22	1.006	5.82E−03
PS_8	0.765	4.84E−02	0.966	6.26E−03	4.21E−02	2.96	0.300	0.058	0.276	1.31E−02	5.43	1.057	3.30E−03
PS_8 + bulk	0.771	4.67E−02	0.960	7.30E−03	3.94E−02	2.15	0.466	0.116	0.347	6.87E−03	4.09	0.736	3.85E−03
PS_8 + > 30 kDa	0.798	4.05E−02	0.960	7.37E−03	3.32E−02	1.31	0.334	0.106	0.329	1.05E−02	3.40	0.571	5.52E−03
PS_8 + 10–30 kDa	0.766	4.79E−02	0.961	7.19E−03	4.08E−02	0.84	0.353	0.039	0.338	1.13E−02	4.07	0.732	5.55E−03
PS_8 + 3–10 kDa	0.731	5.60E−02	0.962	6.99E−03	4.90E−02	2.31	0.587	0.073	0.342	1.44E−02	4.65	0.871	6.54E−03
PS_8 + < 3 kDa	0.728	5.67E−02	0.962	6.98E−03	4.97E−02	4.71	0.741	0.138	0.337	1.75E−02	6.01	1.194	5.78E−03

equilibrium-kinetic model, which also well described the BTCs (Figure S9). The initial retardation, as indicated by high R and K_r, reflected the rapid, instantaneous retention of NPs during the first stage. As particle accumulation continued, the sand surface reached its apparent equilibrium, leading to breakthrough. Subsequently, NP attachment during the plateau (k_{att}) was primarily governed by slow kinetic irreversible attachment, consistent with k_{a2} in the two-site kinetic model. Overall, the modeling further supports a two-stage deposition process of NPs: an initial stage characterized by a low amount of fast, reversible or pseudo-equilibrium attachment until site saturation, followed by a subsequent stage dominated by slow, irreversible attachment.

3.2. Sand surface heterogeneity creates favorable deposition sites

Typically, primary and secondary energy minima can produce irreversible and reversible deposition sites, with primary-minimum deposition being much more stable than secondary-minimum deposition [10,53]. Based on DLVO theory calculations (Figure S10), a relatively high energy barrier (220 k_BT) was observed for NP-sand interactions, making it difficult for the NPs to diffuse over these barriers into the primary energy minimum [54]. The shallow secondary energy minimum of −0.145 k_BT suggests that only limited NP deposition might occur. Therefore, the visible retardation of BTC and site blocking of PS NPs could not be explained by the classical DLVO theory, although the interaction energy only represents the average value between NPs and sand surfaces. For a homogeneous surface, the attachment potential predicted by the interaction energy would result in a constant deposition rate. However, natural sands are typically physically and chemically heterogeneous, leading to variations in the interaction energies between particles and different locations on the heterogeneous surfaces [55], which might explain the deviation from the classical DLVO and CFT.

To elucidate the underlying mechanism behind the observed retardation phenomenon, the transport behavior of PS NPs in 10 mM NaCl was tested using sands from various sources, as shown in Fig. 2a. Site blocking was observed across all types of sands; however, differences in retardation were evident. Specifically, negligible retardation occurred in Sigma−1 sands with diameters of 0.425–0.6 mm and 0.2–0.425 mm, whereas considerable retardation was observed in the 0.210–0.297 mm Sigma−2 sand, similar to the behavior seen with vidaXL sand. SEM images exhibited that the surface of Sigma−1 sand was relatively smooth, with regular shallow scratches or grooves (Figs. 2c and 2d). However, the surfaces of vidaXL sand and Sigma−2 sand exhibited numerous irregularities and pronounced unevenness. Most NPs tended to accumulate at these rough sites, suggesting that physical heterogeneity was likely responsible for the retardation of NPs in vidaXL and Sigma−2 sand (Figs. 2b and 2e). In a previous study [56], we observed a similar phenomenon, where retardation of silver nanoparticles occurred in rough sand, while negligible retardation was noted in relatively smooth sand.

The surface roughness of sand including protruding asperities and concave areas can create favorable sites for NP attachment under unfavorable conditions [13,14]. As calculated, the energy barrier decreased from 220 k_BT to 84.6 k_BT, 44.1 k_BT, and 33.5 k_BT in the presence of 50 nm, 20 nm, and 10 nm convex asperities, respectively (Figure S10a1). Irreversible attachment at the primary energy minimum may be enhanced at the tops of nanoscale protruding asperities [55]. In contrast, within the concave valleys between asperities of these sizes, the secondary minimum depth increased from 0.145 k_BT to 0.629 k_BT, 0.583 k_BT, and 0.507 k_BT, respectively (Figure S10b2). It indicated that concave areas enhance reversible attachment at the secondary energy minimum by increasing its depth [10,45]. Beyond this, concave areas may also reduce hydrodynamic drag forces, thereby enabling irreversible attachment [10]. Studies further indicate that colloid immobilization under unfavorable conditions may arise from wedging within grain-grain junctions [57,58]. Instead of overcoming the energy barrier, colloids may migrate along collector surfaces via secondary-minimum interactions until they become immobilized in

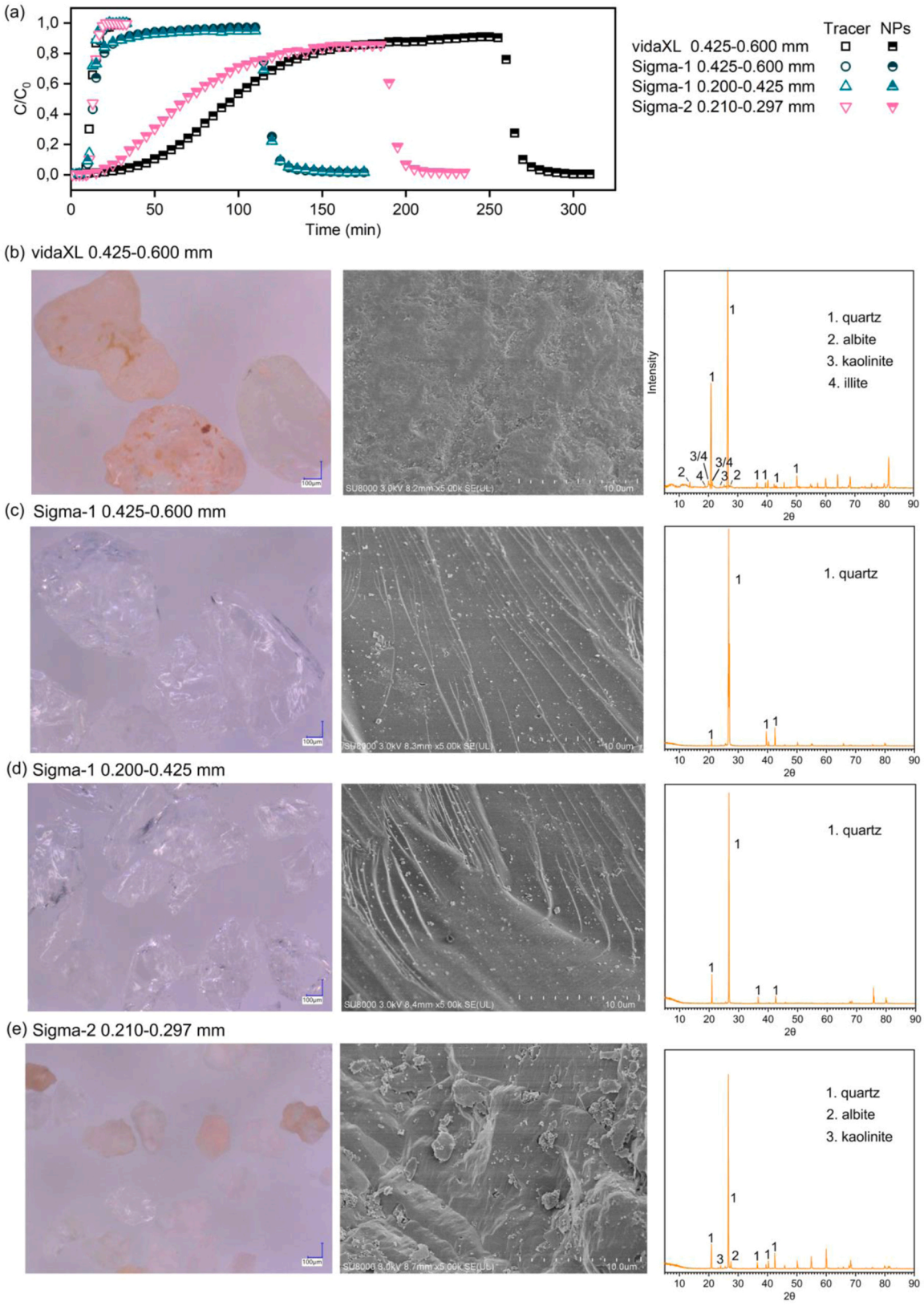

Fig. 2. (a) BTCs of tracer and NPs in different types of sand; microscopic images of the sand, SEM images showing NP deposition on sand surfaces, and XRD spectra of the sands: (b) vidaXL 0.525–0.600 mm, (c) Sigma−1 0.425–0.600 mm, (d) Sigma−1 0.200–0.425 mm, and (e) Sigma−2 0.210–0.297 mm.

regions with reduced hydrodynamic shear, such as interstitial spaces between grains [57,58].

In addition, microscopic analyses showed that the 0.425–0.6 mm and 0.2–0.425 mm Sigma−1 sands were clean and transparent with no visible impurities, whereas the 0.210–0.297 mm Sigma−2 sand and vidaXL sand exhibited colored hues (Figs. 2b-2e). Despite sequential treatments with HCl, NaOH, and thermal combustion to remove metal oxides and organic impurities, certain clay minerals might have remained due to their resistance to these treatments [59]. SEM-EDS and XRD analyses confirmed the potential presence of minerals in vidaXL sand (albite, kaolinite, and illite) and in the 0.210–0.297 mm Sigma−2 sand (albite and kaolinite) (Figure S11, 2b, and 2e) [60]. The presence of minerals was also associated with the less negative zeta potential of vidaXL sand (-41.7 ± 0.8 mV) and 0.210–0.297 mm Sigma−2 sand (-40.4 ± 0.7 mV) compared to the 0.425–0.6 mm (-45.5 ± 0.5 mV) and 0.2–0.425 mm (-46.8 ± 1.3 mV) Sigma−1 sands (Figure S12), likely due to positively charged edge positions such as Al^{3+} [61–63]. Considering the chemical heterogeneity, the energy barrier decreased from 220 k_BT to 163 k_BT, 119 k_BT, and 34.1 k_BT in the presence of a positively charged area (e.g., + 40 mV) with size of 10 nm, 20 nm, and 50 nm, respectively (Figure S10c1), likely promoting irreversible attachment at the primary energy minimum. Concurrently, the secondary energy minimum increased from 0.145 k_BT to 0.155 k_BT, 0.165 k_BT, and 0.217 k_BT (Figure S10c2), enhancing the likelihood for irreversible attachment as hydrodynamic drag forces became less influential. Although previous studies did not explicitly mention retardation, the findings have suggested a potential link between the observed retardation of colloids and the presence of clay minerals [59,63,64]. For instance, increasing contents of clay minerals such as kaolinite, montmorillonite, and illite have appeared to cause more retardation of NPs [63–65]. Using the same 0.210–0.297 mm Sigma−2 sand, retardation has also been observed for PS NPs [27], and graphene oxide nanoparticles [66].

Consequently, the combined physical and chemical heterogeneity of sand surfaces in sand can lead to a wide distribution of primary and/or secondary minimum depths as well as attenuated hydrodynamic shear forces, which may contribute to the observed breakthrough behavior of NPs. As reported, attachment to kinetically limited sites may occur in the primary energy minimum where overcoming an energy barrier is required, while attachment to fast equilibrium sites may take place in the secondary energy minimum [67]. In the initial stage, surface heterogeneity may create numerous favorable locations for both rapid reversible (less important) and irreversible (dominant process) NP attachment at these energy minima, leading to initial NP retardation. As these high-affinity sites become saturated, they may be no longer available for further attachment, resulting in site blocking. Subsequently, during the second or third NP pulses, incoming NPs may deposit predominantly onto relatively smooth surfaces, where irreversible

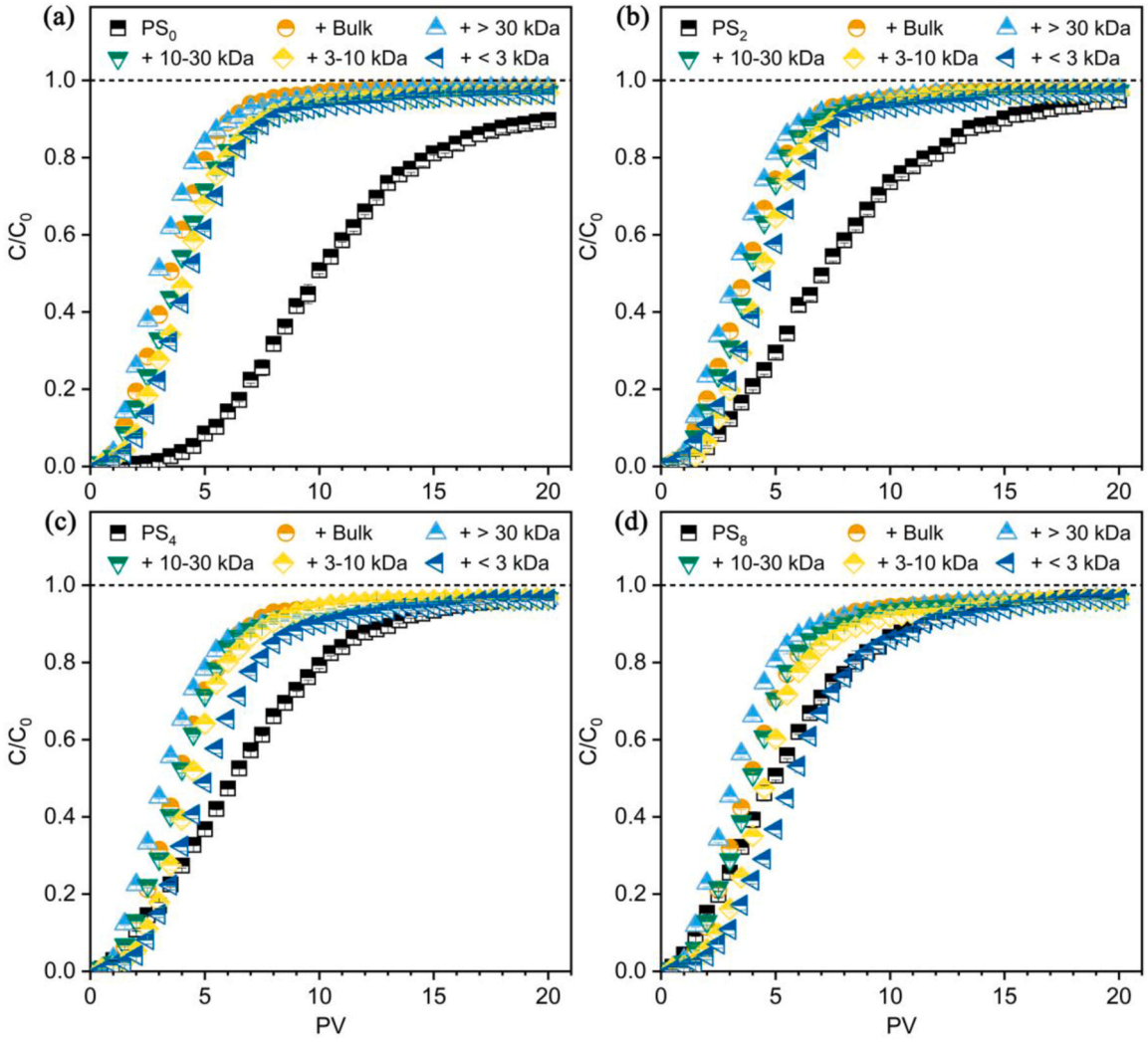

Fig. 3. The BTCs of non-weathered and UV-weathered NPs in the absence and presence of bulk NOM and NOM fractions (2 mg C/L) in 10 mM NaCl. Subscripts 0, 2, 4 and 8 mean aging times of 0, 2, 4 and 8 d. Error bars represent the mean ± range (minimum to maximum) (n = 2).

attachment at the primary energy minimum dominates [53,68].

3.3. UV weathering reduces surface heterogeneity effects

The BTCs for both pristine and UV-weathered NPs in sand columns are depicted in Fig. 3. Compared to the pristine NPs, the UV-weathered NPs exhibited earlier breakthrough. The concentration plateau was reached faster as the aging time increased, indicating that photo-oxidation enhanced NP mobility (Table 1). The equilibrium-kinetic model and two-site kinetic model also accurately described the transport of UV-weathered NPs (Figure S9). The reduction in K_d from an initial value of 2.15 mL/g to 1.54 mL/g, 1.37 mL/g and 1.06 mL/g indicates that the retention capacity of sand for PS NPs decreased with UV weathering. This trend was consistent with the batch experiments, where the removal of NPs after 48 h decreased from 82.0% for PS_0 to 58.0%, 49.9%, and 32.8% for PS_2, PS_4, and PS_8, respectively (Figure S6). The initial k_{a1} value of 1.038 min^{-1} for PS_0 reduced to 0.464 min^{-1}, 0.328 min^{-1}, and 0.300 min^{-1} for PS_2, PS_4, and PS_8, respectively. The same trend was observed for k_{a2} and k_{att}. Correspondingly, S_{max1} exhibited a decrease from 8.84 μg/g for PS_0 to 6.12 μg/g, 3.01 μg/g, and 2.96 μg/g for PS_2, PS_4, and PS_8, respectively, while S_{max2} dropped from 0.632 μg/g for PS_0 to 0.391 μg/g, 0.310 μg/g, and 0.276 μg/g for PS_2, PS_4, and PS_8, respectively. Similar to pristine NPs, multi-site deposition was observed for UV-weathered NPs; however, the number of available sites was lower compared to the pristine NPs. This reduction likely reflected changes in surface properties of the NPs, impacting their interaction dynamics with the collector surfaces.

As shown in Fig. 4a, UV weathering increased oxygen-containing functional groups on NP surfaces, resulting in more negatively charged particles (Fig. 4e). Consequently, the increased electrostatic repulsion between the NPs and sand could be a contributing factor for the reduced retention [25]. Table 2 shows the energy barrier and secondary energy minimum between NPs and heterogeneous/homogeneous surfaces. Although surface roughness greatly reduced the energy barriers, the barriers between UV-weathered NPs and convex asperity (e.g., 10 nm) (46.1–52.4 k_BT) remained higher than those for pristine NPs (33.5 k_BT). Meanwhile, the secondary minimum between NPs and concave valley decreased (0.090–0.196 k_BT vs. 0.507 k_BT). Although the presence of positively charged areas may favor the attachment of more negatively charged UV-weathered NPs, DLVO calculations still predicted higher energy barriers (54.2–96.2 k_BT vs. 34.1 k_BT) and shallower secondary minima (0.038–0.079 k_BT vs. 0.217 k_BT) between UV-weathered NPs and a positively charged area (e.g., 50 nm, + 40 mV) (Table 2), due to the dominant influence of the surrounding negatively charged surface. It indicates that UV weathering reduced both irreversible deposition at the primary energy minimum and reversible deposition at the secondary energy minimum. Furthermore, UV weathering rendered these originally favorable heterogeneous sites for non-weathered NPs unfavorable, leading to the reduced retardation and the rapid reaching of the steady-state plateau observed in the BTCs of UV-weathered NPs. Although not emphasized by the respective authors, carboxyl group-functionalized NPs that mimic weathered NPs, exhibited negligible retardation compared to their non-functionalized counterparts when transported through Sigma sand with an average diameter of 0.260 mm [27] Therefore, UV weathering can reshape NP surface properties, reducing the influence of sand surface heterogeneity and causing NPs to undergo distinct transport dynamics.

3.4. NOM reduces surface heterogeneity effects

The retardation of pristine NPs decreased in the presence of NOM, as evidenced by the rapid breakthrough of NPs at first PV (Fig. 3). After

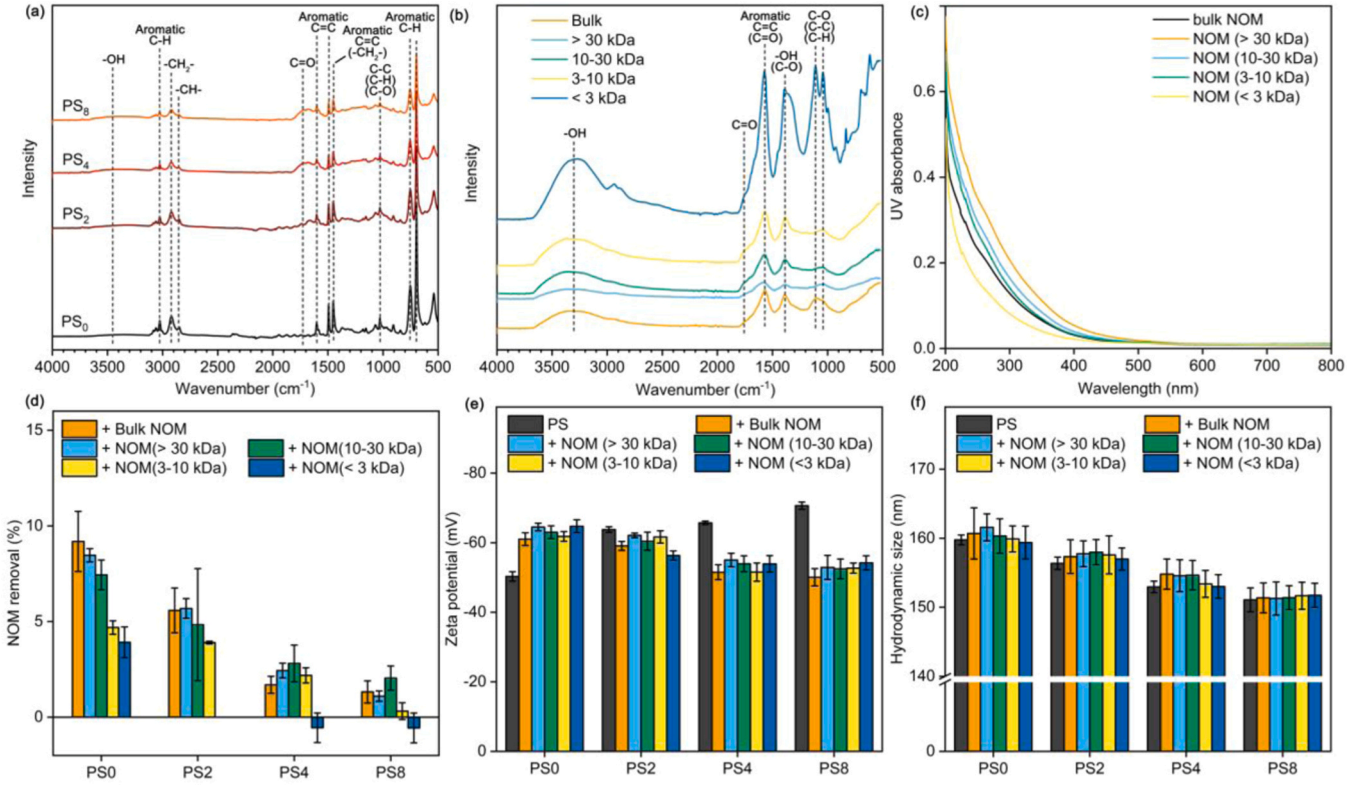

Fig. 4. (a) FTIR spectra of pristine and photoaged NPs. (b) FTIR spectra of bulk NOM and NOM fractions. (c) UV absorbance of bulk NOM and different NOM fractions (4 mg C/L). (d) The reduction in UV280 (NOM removal) of bulk NOM and NOM fractions after adsorption on pristine and photoaged NPs in 10 mM NaCl. Error bars represent the mean ± range (minimum to maximum) (n = 2). (d) The zeta potential of pristine and photoaged NPs with and without bulk NOM and NOM fractions in 10 mM NaCl (f). Error bars represent the mean ± 1.96 SE (n = 10). (e) The hydrodynamic size of pristine and photoaged NPs with and without bulk NOM and NOM fractions in 10 mM NaCl. Error bars represent the mean ± 1.96 SE (n = 10). Subscripts 0, 2, 4 and 8 mean aging times of 0, 2, 4 and 8 d.

Table 2
The DLVO and XDLVO energy barrier (E_{max}, k_BT) and the secondary minimum ($|E_{2\text{-}min}|$, k_BT) for NP–asperity and NP–valley (assuming a 10 nm asperity), and NP-positively charged area on heterogeneous surface (assuming a +40 mV region with a diameter of 50 nm) and NP-plate on homogeneous surface.

NP-Sand	Heterogeneous Surface						Homogeneous Surface	
	NP-asperity		NP-valley		NP-positively charged area		NP-plate	
	E_{max}	$\lvert E_{2\text{-}min} \rvert$	E_{max}	$\lvert E_{2\text{-}min} \rvert$	E_{max}	$\lvert E_{2\text{-}min} \rvert$	E_{max}	$\lvert E_{2\text{-}min} \rvert$
PS_0	33.5	0.135	774	0.507	34.1	0.217	220	0.145
PS_0 + bulk	177	0.131	3900	0.487	1216	0.206	1480	0.140
PS_0 + > 30 kDa	348	0.129	7761	0.483	2737	0.203	3013	0.138
PS_0 + 10–30 kDa	170	0.130	3759	0.485	1145	0.205	1414	0.139
PS_0 + 3–10 kDa	61.7	0.130	1381	0.486	197	0.206	450	0.140
PS_0 + < 3 kDa	47.4	0.129	1078	0.482	66.8	0.203	320	0.138
PS_2	46.1	0.053	1063	0.196	54.2	0.079	300	0.056
PS_2 + bulk	98.4	0.054	2186	0.199	508	0.081	762	0.057
PS_2 + > 30 kDa	201	0.053	4461	0.197	1392	0.080	1659	0.056
PS_2 + 10–30 kDa	103	0.054	2301	0.198	546	0.080	804	0.056
PS_2 + 3–10 kDa	62.4	0.053	1403	0.197	186	0.080	443	0.056
PS_2 + < 3 kDa	46.9	0.054	1063	0.200	81.3	0.082	316	0.057
PS_4	49.0	0.031	1120	0.113	57.3	0.045	315	0.032
PS_4 + bulk	58.0	0.032	1296	0.117	189	0.047	411	0.033
PS_4 + > 30 kDa	71.2	0.032	1592	0.116	286	0.047	520	0.033
PS_4 + 10–30 kDa	61.9	0.032	1386	0.117	211	0.047	441	0.033
PS_4 + 3–10 kDa	46.7	0.032	939	0.118	96.2	0.047	314	0.033
PS_4 + < 3 kDa	42.9	0.032	976	0.117	56.4	0.047	279	0.033
PS_8	52.4	0.024	1195	0.090	60.6	0.035	335	0.025
PS_8 + bulk	57.5	0.026	1281	0.095	189	0.038	405	0.027
PS_8 + > 30 kDa	62.4	0.025	1394	0.094	218	0.037	443	0.027
PS_8 + 10–30 kDa	58.9	0.026	1316	0.094	189	0.037	414	0.027
PS_8 + 3–10 kDa	43.1	0.025	947	0.096	61.3	0.037	279	0.027
PS_8 + < 3 kDa	42.1	0.025	922	0.095	48.6	0.037	269	0.026

NOM addition, the attachment efficiencies α_1 and α_2 reduced from 0.079 and 0.015–0.030 and 0.003, respectively, corresponding to the reduction in K_d and k_{att} in the equilibrium-kinetic model. Based on the two-site model fitting, the parameters S_{max1} and S_{max2} decreased from 8.84 μg/g and 0.632 μg/g to 0.720 μg/g and 0.161 μg/g after the addition of NOM, indicating that NP deposition on both heterogeneous and homogeneous surfaces decreased. Batch adsorption experiments revealed that 9% of NOM adsorbed onto PS NPs (Fig. 4d). Additionally, the adsorption of NOM greatly increased the negative charge of the pristine NPs (Fig. 4e), probably due to the charge superposition of the adsorbed NOM [69,70]. The increase in electrostatic repulsion likely explains the enhanced mobility of NPs in the presence of NOM [23]. Steric repulsion due to NOM adsorption is typically considered a key factor contributing to increased mobility of engineered colloids in porous media, such as graphene oxide [71], ZnO [72], and Ag [73], as well as PS NPs [19,27]. In this study, steric repulsion likely played a critical role in increasing the mobility of PS NPs as well. According to XDLVO theory, NOM adsorption greatly increased the energy barrier between NPs and sand surfaces (Table 2), thereby reducing the irreversible deposition of NPs.

Similar to pristine NPs, the deposition of UV-weathered NPs on heterogeneous and homogeneous surfaces reduced in the presence of NOM, as indicated by reductions in the fitted parameters k_{a1}, k_{a2}, S_{max1} and S_{max2}, as well as K_d and k_{att}. In contrast to the pristine NPs, the zeta potential of UV-weathered NPs, especially PS_4 and PS_8, became less negative in the presence of NOM (Fig. 4f). Limited studies have reported this phenomenon, but we propose that the reduction in negative charges may be attributed to the shielding of charges or oxygen-containing groups on UV-weathered NPs by NOM [29]. Furthermore, this effect was more pronounced as UV aging time increased, due to the generation of more surface oxygen-containing groups on the more weathered NPs (Fig. 4f). Although NOM could decrease the electrostatic repulsion between UV-weathered NPs and the sand, steric repulsion may outweigh the effects of reduced electrostatic interaction. XDLVO theory suggested that NOM-induced short-distance steric repulsion primarily affected the energy barriers between UV-weathered NPs and both heterogeneous and homogeneous surfaces, with minimal impact on the secondary energy minimum (Table 2). This led to a reduction in the irreversible deposition of UV-weathered NPs at the primary energy minimum.

Similar to UV weathering, the weathering of NPs by NOM also diminished the effect of sand surface heterogeneity on NP transport and greatly reduced retardation. Different effects of NOM on NP transport dynamics have been identified in previous studies, although not explicitly highlighted. For instance, on standard quartz sand and glass beads, NPs have exhibited a steady-state breakthrough, and model NOM compounds such as humic acid, bovine serum albumin, and sodium alginate have been found to only enhance the height of the BTC plateau without altering the overall transport dynamics [26,74]. However, in the study by Zhu et al., retardation of pristine NPs has been observed in Sigma sand (0.260 mm), while NOM components such as fulvic acid, humic acid, and macromolecular extracellular polymeric substances (EPS) have been found to reduce this retardation. In particular, EPS appeared to eliminate retardation entirely, resulting in a near steady-state breakthrough [27]. Similarly, low-molecular-weight organic acids have been observed to reduce the retardation of NPs in columns using sand sourced from Tianjin Guangfu Technology Development Co., Ltd. Chen et al., [75]. These findings highlight the complex interplay between NP weathering by NOM and sand surface heterogeneity in shaping NP transport.

3.5. NOM molecular weight-dependent deposition of nanoplastics

NOM is a heterogeneous group of compounds with varying MW and chemical properties [76]. The MW of NOM could determine its reactivity with NPs and control their mobility in porous media [27]. For pristine NPs in the presence of NOM fractions, the attachment efficiencies α, α_1 and α_2 generally decreased as the MW of NOM increased, indicating that mostly the higher-MW NOM increased NP mobility. In the equilibrium-kinetic model, the K_d value increased from 0.534 mL/g to 0.718 mL/g, 0.776 mL/g, and 0.832 mL/g, and k_{att} increased from 0.0034 min^{-1}, 0.0034 min^{-1}, 0.0046 min^{-1}, 0.0048 min^{-1} as NOM MW decreased. Similarly, k_{a1}, S_{max1}, S_{max2} decreased with increasing NOM MW, whereas k_{a2} showed no obvious correlation. This suggests that NOM with a higher MW had a stronger capacity to reduce the deposition of NPs.

As shown in Figs. 4b and 4c, higher-MW NOM exhibited fewer oxygen-containing functional groups but greater aromaticity, which could favor adsorption onto hydrophobic PS surfaces through hydrophobic and π–π interactions [29]. Batch adsorption experiments further showed that higher-MW NOM exhibited greater adsorption onto pristine NPs (Fig. 4d). Although the difference was not statistically significant, the hydrodynamic size of NPs was slightly larger in the presence of higher-MW NOM compared to lower-MW NOM (Fig. 4f). The higher adsorption and larger molecular size of higher-MW NOM may enhance steric repulsion, thereby increasing the mobility of pristine NPs compared to lower-MW NOM. XDLVO theory revealed that the energy barriers between NPs and sand surfaces increased with higher NOM MW, while the secondary energy minima between NPs and sand surfaces remained nearly unchanged across different NOM MWs (Table 2). Therefore, NOM MW primarily influenced the availability of irreversible deposition sites on heterogeneous and homogeneous surfaces.

For UV-weathered NPs, a similar trend was observed, with higher mobility in the presence of higher MW NOM. However, not all MW NOMs enhanced the mobility of UV-weathered NPs. As evidenced by the increase in attachment efficiencies α, the presence of < 3 kDa and 3–10 kDa NOM reduced the mobility of PS_4 and PS_8. Although all NOM fractions reduced the negative charges of UV-weathered NPs (Fig. 4e), the adsorption of lower MW NOM (e.g., < 3 kDa) on PS_4 and PS_8 was negligible (Fig. 4d). This suggests that steric repulsion induced by lower-MW NOM on PS4 and PS8 is very weak. We therefore propose that a competition between electrostatic interaction and steric repulsion was at play. In the presence of higher MW NOM, the additional steric repulsion outweighed the reduced electrostatic repulsion, leading to enhanced mobility of UV-weathered NPs. Conversely, with lower MW NOM, the reduced electrostatic repulsion dominated, resulting in increased deposition of PS_4 and PS_8. According to XDLVO predictions, the energy barrier between PS_8 and convex asperity increased from 52.4 k_BT to 62.4 and 58.9 k_BT in the presence of > 30 kDa and 10–30 kDa NOM, respectively, but decreased to 43.1 and 42.1 k_BT in the presence of 3–10 kDa and < 3 kDa NOM, respectively (Table 2). On smooth surfaces, the energy barriers remained high (> 260 k_BT) both in the absence and presence of NOM fractions. Therefore, the influence of NOM and its fractions on the irreversible deposition of UV-weathered NPs primarily occurred on these heterogeneous surfaces.

4. Conclusions and implications

This study focused on the deposition mechanisms of non-weathered and weathered PS NPs in saturated porous media under typically low ionic strength conditions. Our findings reveal that the transport dynamic of NPs deviated from traditional CFT and DLVO theory. Instead, a two-stage transport with mostly irreversible and to a lesser degree also reversible attachment was observed, particularly for non-weathered NPs during the first filtration pulse. This retardation behavior is not emphasized in other studies due to their different research objectives [20,23,59], and it may resemble steady-state transport with a very low breakthrough when breakthrough curves are measured over short timeframes and/or at low concentrations of NPs. These results highlight the importance of considering the full breakthrough curve, especially during the first filtration pulse.

The study also reveals the critical role of sand grain physical and chemical heterogeneity in this two-stage transport of NPs. It suggests that clean, ideal quartz sands or glass beads are inadequate representations of natural sands in transport studies. Additionally, this study underscores the role of natural weathering in reshaping the transport behaviors of NPs, particularly in masking the influence of sand surface heterogeneity on retardation. To better reflect real-world scenarios, future studies should prioritize the use of natural heterogeneous porous media and weathered NPs.

However, several limitations remain in this study. The experiments were conducted under simplified and controlled conditions to explore the effects of sand heterogeneity and NP weathering on NP transport dynamics. Other factors, such as NP size and polymer type, ionic strength and composition, and the presence of clay minerals, microorganisms, biofilms, and natural colloids, were not considered. Therefore, caution should be exercised when extrapolating these findings to more complex environmental systems, where multiple physicochemical and biological processes may interact. In addition, characterization of sand surfaces is largely qualitative due to current analytical limitations. The interaction calculations are also based on idealized assumptions and are intended to provide a qualitative understanding of NP–sand interactions, rather than quantitatively precise predictions of interaction energies under environmental conditions.

Environmental implication

This study demonstrates that natural weathering processes fundamentally alter nanoplastic transport in porous media by reducing surface heterogeneity–driven retention. Weathered nanoplastics exhibit enhanced mobility and diminished retardation, increasing their likelihood of penetrating subsurface environments and reaching groundwater. The findings challenge conventional filtration and transport models that neglect surface heterogeneity and weathering effects. Moreover, the dependence on natural organic matter characteristics highlights the complexity of nanoplastic behavior in real waters. These results underscore the need to incorporate weathering and environmental variability into risk assessments and to reassess the effectiveness of natural and engineered filtration systems in controlling nanoplastic pollution.

CRediT authorship contribution statement

Lompe Kim: Writing – review & editing, Writing – original draft, Supervision, Project administration, Funding acquisition, Formal analysis, Conceptualization. **Gang Liu:** Writing – review & editing, Writing – original draft, Supervision, Project administration, Funding acquisition, Conceptualization. **Yanghui Xu:** Writing – original draft, Visualization, Investigation, Formal analysis, Conceptualization. **Rietveld Luuk:** Writing – review & editing, Supervision. **van der Hoek Jan:** Writing – review & editing, Supervision.

Declaration of Competing Interest

The authors declare that they have no known competing financial interests or personal relationships that could have appeared to influence the work reported in this paper.

Acknowledgements

The present work has been financially supported by the National Natural Science Foundation of China (grant no. 52525003).

Appendix A. Supporting information

Supplementary data associated with this article can be found in the online version at doi:10.1016/j.jhazmat.2026.142872.

Data availability

Data will be made available on request.

References

[1] Liu, W., Zhao, Y., Shi, Z., Li, Z., Liang, X., 2020. Ecotoxicoproteomic assessment of microplastics and plastic additives in aquatic organisms: a review. Comp Biochem Physiol Part D Genom Proteom 36, 100713.
[2] Simon-Sanchez, L., Grelaud, M., Lorenz, C., Garcia-Orellana, J., Vianello, A., Liu, F., et al., 2022. Can a sediment core reveal the plastic age? Microplastic

preservation in a coastal sedimentary record. Environ Sci Technol 56 (23), 16780–16788.
[3] Wu, M., Zhong, H., 2025. Airborne micro- and nanoplastics: hidden vectors for human infection? New Contam 1, 1.
[4] Zhou, Y., He, G., Bhagwat, G., Palanisami, T., Yang, Y., Liu, W., et al., 2023. Nanoplastics alter ecosystem multifunctionality and may increase global warming potential. Glob Chang Biol 29 (14), 3895–3909.
[5] Bhardwaj, L.K., Rath, P., Choudhury, M., 2023. A comprehensive review on the classification, uses, sources of nanoparticles (NPs) and their toxicity on health. Aerosol Sci Eng 7 (1), 69–86.
[6] Shi, Y., Zheng, L., Huang, H., Tian, Y.C., Gong, Z., Liu, P., et al., 2023. Formation of Nano- and Microplastics and Dissolved Chemicals During Photodegradation of Polyester Base Fabrics with Polyurethane Coating. Environ Sci Technol 57 (5), 1894–1906.
[7] Xu, Y., Ou, Q., Jiao, M., Liu, G., van der Hoek, J.P., 2022. Identification and Quantification of Nanoplastics in Surface Water and Groundwater by Pyrolysis Gas Chromatography-Mass Spectrometry. Environ Sci Technol 56 (8), 4988–4997.
[8] Babakhani, P., Bridge, J., Doong, R.A., Phenrat, T., 2017. Continuum-based models and concepts for the transport of nanoparticles in saturated porous media: A state-of-the-science review. Adv Colloid Interface Sci 246, 75–104.
[9] Harvey, R.W., Garabedian, S.P., 1991. Use of colloid filtration theory in modeling movement of bacteria through a contaminated sandy aquifer. Environ Sci Technol 25 (1), 178–185.
[10] Shen, C., Jin, Y., Zhuang, J., Li, T., Xing, B., 2019. Role and importance of surface heterogeneities in transport of particles in saturated porous media. Crit Rev Environ Sci Technol 50 (3), 244–329.
[11] Adamczyk, Z., Weroński, P., 1999. Application of the DLVO theory for particle deposition problems. Adv Colloid Interface Sci 83 (1-3), 137–226.
[12] Hu, Z., Zhao, J., Gao, H., Nourafkan, E., Wen, D., 2017. Transport and Deposition of Carbon Nanoparticles in Saturated Porous Media. Energies 10 (8), 1151.
[13] Lim, M., Hwang, G., Bae, S., Jang, M.H., Choi, S., Kim, H., et al., 2020. Transport of citrate-coated silver nanoparticles in saturated porous media. Environ Geochem Health 42 (6), 1753–1766.
[14] Sasidharan, S., Torkzaban, S., Bradford, S.A., Dillon, P.J., Cook, P.G., 2014. Coupled effects of hydrodynamic and solution chemistry on long-term nanoparticle transport and deposition in saturated porous media. Colloids Surf A Physicochem Eng Asp 457, 169–179.
[15] El Badawy, A.M., Hassan, A.A., Scheckel, K.G., Suidan, M.T., Tolaymat, T.M., 2013. Key factors controlling the transport of silver nanoparticles in porous media. Environ Sci Technol 47 (9), 4039–4045.
[16] Tufenkji, N., 2007. Modeling microbial transport in porous media: Traditional approaches and recent developments. Adv Water Resour 30 (6-7), 1455–1469.
[17] Cameron, D.R., Klute, A., 1977. Convective dispersive solute transport with a combined equilibrium and kinetic adsorption model. Water Resour Res 13 (1), 183–188.
[18] Praetorius, A., Tufenkji, N., Goss, K.-U., Scheringer, M., von der Kammer, F., Elimelech, M., 2014. The road to nowhere: equilibrium partition coefficients for nanoparticles. Environ Sci Nano 1 (4), 317–323.
[19] Dong, Z., Hou, Y., Han, W., Liu, M., Wang, J., Qiu, Y., 2020. Protein corona-mediated transport of nanoplastics in seawater-saturated porous media. Water Res 182, 115978.
[20] He, L., Rong, H., Wu, D., Li, M., Wang, C., Tong, M., 2020. Influence of biofilm on the transport and deposition behaviors of nano- and micro-plastic particles in quartz sand. Water Res 178, 115808.
[21] Liang, Y., Luo, Y., Shen, C., Bradford, S.A., 2022. Micro- and nanoplastics retention in porous media exhibits different dependence on grain surface roughness and clay coating with particle size. Water Res 221, 118717.
[22] Liu, J., Zhang, T., Tian, L., Liu, X., Qi, Z., Ma, Y., et al., 2019. Aging Significantly Affects Mobility and Contaminant-Mobilizing Ability of Nanoplastics in Saturated Loamy Sand. Environ Sci Technol 53 (10), 5805–5815.
[23] Ma, J., Qiu, Y., Zhao, J., Ouyang, X., Zhao, Y., Weng, L., et al., 2022. Effect of Agricultural Organic Inputs on Nanoplastics Transport in Saturated Goethite-Coated Porous Media: Particle Size Selectivity and Role of Dissolved Organic Matter. Environ Sci Technol 56, 3524–3534.
[24] Mitzel, M.R., Sand, S., Whalen, J.K., Tufenkji, N., 2016. Hydrophobicity of biofilm coatings influences the transport dynamics of polystyrene nanoparticles in biofilm-coated sand. Water Res 92, 113–120.
[25] Ren, Z., Gui, X., Wei, Y., Chen, X., Xu, X., Zhao, L., et al., 2021. Chemical and photo-initiated aging enhances transport risk of microplastics in saturated soils: Key factors, mechanisms, and modeling. Water Res 202, 117407.
[26] Tan, M., Liu, L., Zhang, M., Liu, Y., Li, C., 2021. Effects of solution chemistry and humic acid on the transport of polystyrene microplastics in manganese oxides coated sand. J Hazard Mater 413, 125410.
[27] Zhu, M., Zhang, Z., Zhang, T., Hofmann, T., Chen, W., 2022. Eco-Corona Dictates Mobility of Nanoplastics in Saturated Porous Media: The Critical Role of Preferential Binding of Macromolecules. Environ Sci Technol 57 (1), 331–339.
[28] Zhang, G., Cui, J., Song, J., Ji, Y., Zuo, Y., Jia, H., et al., 2024. Transport of polystyrene nanoplastics with different functional groups in goethite-coated saturated porous media: Effects of low molecular weight organic acids and physicochemical properties. J Colloid Interface Sci 653 (Pt A), 423–433.
[29] Xu, Y., Wang, X., van der Hoek, J.P., Liu, G., Lompe, K.M., 2025. Natural Organic Matter Stabilizes Pristine Nanoplastics but Destabilizes Photochemical Weathered Nanoplastics in Monovalent Electrolyte Solutions. Environ Sci Technol 59 (3), 1822–1834.
[30] Liu, Y., Huang, Z., Zhou, J., Tang, J., Yang, C., Chen, C., et al., 2020. Influence of environmental and biological macromolecules on aggregation kinetics of nanoplastics in aquatic systems. Water Res 186, 116316.
[31] Wang, J., Zhao, X., Wu, A., Tang, Z., Niu, L., Wu, F., et al., 2021. Aggregation and stability of sulfate-modified polystyrene nanoplastics in synthetic and natural waters. Environ Pollut 268 (Pt A), 114240.
[32] Guo, J., Liu, H., Liu, J., Wang, L., 2014. Ultrafiltration performance of EfOM and NOM under different MWCO membranes: Comparison with fluorescence spectroscopy and gel filtration chromatography. Desalination 344, 129–136.
[33] Taniguchi, M., Kilduff, J.E., Belfort, G., 2003. Modes of Natural Organic Matter Fouling during Ultrafiltration. Environ Sci Technol 37 (8), 1676–1683.
[34] Chandel, A., Faizan, F., Shankar, V., 2023. Assessment of column to particle diameter ratio on the hydraulic conductivity of porous media: Wall effect in Darcy Regime. ISH J Hydraul Eng 29 (4), 437–445.
[35] Liu, G., Fang, Z., Zhong, H., Shi, L., Yang, X., Liu, Z., 2020. Transport of Pseudomonas aeruginosa in Porous Media Mediated by Low-Concentration Surfactants: The Critical Role of Surfactant to Change Cell Surface Hydrophobicity. Water Resour Res 56 (2).
[36] Saiers, J.E., Hornberger, G.M., Liang, L., 1994. First- and second-order kinetics approaches for modeling the transport of colloidal particles in porous media. Water Resour Res 30 (9), 2499–2506.
[37] Tufenkji, N., Elimelech, M., 2004. Correlation equation for predicting single-collector efficiency in physicochemical filtration in saturated porous media. Environ Sci Technol 38 (2), 529–536.
[38] Dale, A.L., Lowry, G.V., Casman, E.A., 2015. Much ado about α: reframing the debate over appropriate fate descriptors in nanoparticle environmental risk modeling. Environmental Science Nano 2 (1), 27–32.
[39] He, F., Zhang, M., Qian, T., Zhao, D., 2009. Transport of carboxymethyl cellulose stabilized iron nanoparticles in porous media: column experiments and modeling. J Colloid Interface Sci 334 (1), 96–102.
[40] Zhang, W., Niu, J., Morales, V.L., Chen, X., Hay, A.G., Lehmann, J., et al., 2010. Transport and retention of biochar particles in porous media: effect of pH, ionic strength, and particle size. Ecohydrology 3 (4), 497–508.
[41] Mattison, N.T., O'Carroll, D.M., Kerry Rowe, R., Petersen, E.J., 2011. Impact of porous media grain size on the transport of multi-walled carbon nanotubes. Environ Sci Technol 45 (22), 9765–9775.
[42] Huangfu, X., Xu, Y., Liu, C., He, Q., Ma, J., Ma, C., et al., 2019. A review on the interactions between engineered nanoparticles with extracellular and intracellular polymeric substances from wastewater treatment aggregates. Chemosphere 219, 766–783.
[43] Xu, Y., Ou, Q., Liu, C., Zhou, X., He, Q., Wu, Z., et al., 2020. Aggregation and deposition behaviors of dissolved black carbon with coexisting heavy metals in aquatic solution. Environmental Science Nano 7 (9), 2773–2784.
[44] Shen, C., Wang, F., Li, B., Jin, Y., Wang, L.P., Huang, Y., 2012. Application of DLVO energy map to evaluate interactions between spherical colloids and rough surfaces. Langmuir 28 (41), 14681–14692.
[45] Shen, C., Wang, L.-P., Li, B., Huang, Y., Jin, Y., 2012. Role of Surface Roughness in Chemical Detachment of Colloids Deposited at Primary Energy Minima. Vadose Zone J 11 (1).
[46] Bradford, S.A., Yates, S.R., Bettahar, M., Simunek, J., 2002. Physical factors affecting the transport and fate of colloids in saturated porous media. Water Resour Res 38 (12), 63–61-63-12.
[47] Raychoudhury, T., Tufenkji, N., Ghoshal, S., 2012. Aggregation and deposition kinetics of carboxymethyl cellulose-modified zero-valent iron nanoparticles in porous media. Water Res 46 (6), 1735–1744.
[48] Chowdhury, I., Hong, Y., Honda, R.J., Walker, S.L., 2011. Mechanisms of TiO2 nanoparticle transport in porous media: role of solution chemistry, nanoparticle concentration, and flowrate. J Colloid Interface Sci 360 (2), 548–555.
[49] Kasel, D., Bradford, S.A., Simunek, J., Heggen, M., Vereecken, H., Klumpp, E., 2013. Transport and retention of multi-walled carbon nanotubes in saturated porous media: effects of input concentration and grain size. Water Res 47 (2), 933–944.
[50] Sun, P., Shijirbaatar, A., Fang, J., Owens, G., Lin, D., Zhang, K., 2015. Distinguishable transport behavior of zinc oxide nanoparticles in silica sand and soil columns. Sci Total Environ 505, 189–198.
[51] Cornelis, G., Kirby, J.K., Beak, D., Chittleborough, D., McLaughlin, M., 2010. A method for determination of retention of silver and cerium oxide manufactured nanoparticles in soils. Environ Chem 7 (3), 298–308.
[52] Cornelis, G., Ryan, B., McLaughlin, M.J., Kirby, J.K., Beak, D., Chittleborough, D., 2011. Solubility and batch retention of CeO2 nanoparticles in soils. Environ Sci Technol 45 (7), 2777–2782.
[53] Shen, C., Li, B., Huang, Y., Jin, Y., 2007. Kinetics of Coupled Primary- and Secondary-Minimum Deposition of Colloids under Unfavorable Chemical Conditions. Environ Sci Technol 41, 6976–6982.
[54] Bradford, S.A., Torkzaban, S., Wiegmann, A., 2011. Pore-scale simulations to determine the applied hydrodynamic torque and colloid immobilization. Vadose Zone J 10 (1), 252–261.
[55] Bradford, S.A., Torkzaban, S., 2013. Colloid interaction energies for physically and chemically heterogeneous porous media. Langmuir 29 (11), 3668–3676.
[56] Liang, Y., Zhou, J., Dong, Y., Klumpp, E., Simunek, J., Bradford, S.A., 2020. Evidence for the critical role of nanoscale surface roughness on the retention and release of silver nanoparticles in porous media. Environ Pollut 258, 113803.
[57] Johnson, W.P., Tong, M., Li, X., 2007. On colloid retention in saturated porous media in the presence of energy barriers: The failure of α, and opportunities to predict η. Water Resour Res 43 (12).

[58] Xu, S., Gao, B., Saiers, J.E., 2006. Straining of colloidal particles in saturated porous media. Water Resour Res 42 (12).
[59] Torkzaban, S., Wan, J., Tokunaga, T.K., Bradford, S.A., 2012. Impacts of bridging complexation on the transport of surface-modified nanoparticles in saturated sand. J Contam Hydrol 136 (137), 86–95.
[60] Fernandez, R., Martirena, F., Scrivener, K.L., 2011. The origin of the pozzolanic activity of calcined clay minerals: A comparison between kaolinite, illite and montmorillonite. Cem Concr Res 41 (1), 113–122.
[61] Muller, S., Fiutowski, J., Rasmussen, M.B., Balic Zunic, T., Rubahn, H.G., Posth, N. R., 2025. Nanoplastic in aqueous environments: The role of chemo-electric properties for nanoplastic-mineral interaction. Sci Total Environ 964, 178529.
[62] Tombácz, E., Szekeres, M., 2006. Surface charge heterogeneity of kaolinite in aqueous suspension in comparison with montmorillonite. Appl Clay Sci 34 (1-4), 105–124.
[63] Ye, X., Cheng, Z., Wu, M., Hao, Y., Lu, G., Hu, B.X., et al., 2022. Effects of clay minerals on the transport of polystyrene nanoplastic in groundwater. Water Res 223, 118978.
[64] Lu, T., Gilfedder, B.S., Peng, H., Niu, G., Frei, S., 2021. Effects of clay minerals on the transport of nanoplastics through water-saturated porous media. Sci Total Environ 796, 148982.
[65] Wu, Y., Cheng, Z., Wu, M., Hao, Y., Lu, G., Mo, C., et al., 2023. Quantification of two-site kinetic transport parameters of polystyrene nanoplastics in porous media. Chemosphere 338, 139506.
[66] Li, J., Chen, J., Lu, T., Wang, Y., Zhang, H., Shang, Z., et al., 2019. Effects of low-molecular weight organic acids on the transport of graphene oxide nanoparticles in saturated sand columns. Sci Total Environ 666, 94–102.
[67] Bales, R.C., Hinkle, S.R., Kroeger, T.W., Stocking, K., Gerba, C.P., 1991. Bacteriophage adsorption during transport through porous media: Chemical perturbations and reversibility. Environ Sci Technol 25 (12), 2088–2095.
[68] Li, T., Jin, Y., Huang, Y., Li, B., Shen, C., 2017. Observed Dependence of Colloid Detachment on the Concentration of Initially Attached Colloids and Collector Surface Heterogeneity in Porous Media. Environ Sci Technol 51 (5), 2811–2820.
[69] Yin, Y., Shen, M., Tan, Z., Yu, S., Liu, J., Jiang, G., 2015. Particle coating-dependent interaction of molecular weight fractionated natural organic matter: impacts on the aggregation of silver nanoparticles. Environ Sci Technol 49 (11), 6581–6589.
[70] Zhang, Y., Chen, Y., Westerhoff, P., Crittenden, J., 2009. Impact of natural organic matter and divalent cations on the stability of aqueous nanoparticles. Water Res 43 (17), 4249–4257.
[71] Shen M., Hai X., Shang Y., Zheng C., Li P., Li Y., Insights into aggregation and transport of graphene oxide in aqueous and saturated porous media: complex effects of cations with different molecular weight fractionated natural organic matter. 656, 843-851.2019.
[72] Jiang X., Tong M., Kim H.J.Joc, science i 2012. Influence of natural organic matter on the transport and deposition of zinc oxide nanoparticles in saturated porous media. 386(1), 34-43..
[73] Kanel S.R., Flory J., Meyerhoefer A., Fraley J.L., Sizemore I.E., Goltz M.N.Influence of natural organic matter on fate and transport of silver nanoparticles in saturated porous media: laboratory experiments and modeling. 17, 1-13.2015.
[74] Tan, M.-M., Feng, L.-J., Bian, S.-Z., Duan, J.-L., Li, X.-H., Sun, X.-D., et al., 2024. Interaction of dissolved organic matters and microplastics regulates the transport of microplastics in saturated porous media. ACS ES&T Eng 4 (5), 1230–1239.
[75] Chen, F., Wei, X., Gong, Y., Chen, D., Lu, T., 2024. Effects of low-molecular-weight organic acids on the transport of polystyrene nanoplastics: An insight at the structure of organic acids. Sci Total Environ 949, 175204.
[76] Louie, S.M., Tilton, R.D., Lowry, G.V., 2013. Effects of molecular weight distribution and chemical properties of natural organic matter on gold nanoparticle aggregation. Environ Sci Technol 47 (9), 4245–4254.